



Selective oxofunctionalization of cyclohexane over titanium dioxide-based and bismuth oxyhalide (BiOX , $\text{X} = \text{Cl}^-$, Br^- , I^-) photocatalysts by visible light irradiation



Adolfo Henríquez^{a,b}, Héctor D. Mansilla^b, Azael Martínez Martínez-de la Cruz^c, Juanita Freer^{a,b}, David Contreras^{a,b,*}

^a Renewable Resources Laboratory, Biotechnology Center, University of Concepción, University Campus, Concepción, Chile

^b Faculty of Chemical Sciences, University of Concepción, University Campus, Concepción, Chile

^c Faculty of Mechanic and Electric Engineering, Autonomous University of Nuevo León, University Village, 66451 San Nicolás de los Garza, NL, Mexico

ARTICLE INFO

Article history:

Received 9 August 2016

Received in revised form

30 December 2016

Accepted 6 January 2017

Available online 9 January 2017

Keywords:

Green chemistry

Photocatalysis

Oxofunctionalization

ABSTRACT

Solar photocatalysis has been employed for pollutant removal by driving the substrates to complete mineralization. These unselective systems can become selective by tuning the reaction conditions and the properties of the photocatalyst for the oxofunctionalization of unreactive compounds such as hydrocarbons.

This work focused on the selective oxofunctionalization of cyclohexane by visible light photocatalysis under ambient conditions. For this purpose, five titanium dioxide-based photocatalysts (Fe-doped TiO_2 , N-doped and undoped TiO_2) and three bismuth oxyhalide photocatalysts (BiOCl , BiOBr and BiOI) were synthesized and characterized (XRD, DRS, SEM and BET surface area). The titanium dioxide-based photocatalysts showed the highest selectivity for cyclohexanone (cyclohexanone/cyclohexanol = 4.49–87.50). BiOCl and BiOBr showed similar yields for cyclohexanone and cyclohexanol production (cyclohexanone/cyclohexanol = 1.92 and 1.27, respectively). The BiOI photocatalysts showed the highest selectivity for cyclohexanol production (cyclohexanone/cyclohexanol = 0.23). The cyclohexanol yield depended linearly on the bandgap of the BiOX . BiOI reached the maximum cyclohexanol yield ($16.5 \pm 1.3 \mu\text{mol m}^{-2} \text{ g}^{-1}$). In all assayed systems, the cyclohexyloxy radical was identified as an intermediate. However, only when BiOI was utilized was there evidence of $\cdot\text{OH}$ radical production. A higher yield of cyclohexanol than cyclohexanone was obtained only by using this photocatalyst. Thus, the selectivity was associated with cyclohexanol production by hydroxylation of the cyclohexyl radical by the $\cdot\text{OH}$ radical.

© 2017 Elsevier B.V. All rights reserved.

1. Introduction

Selective oxidation of hydrocarbons by air (molecular oxygen) is a significant process in the chemical industry that allows relatively cheap hydrocarbons to be converted into valuable oxofunctionalized products, such as feedstocks for both the chemical and pharmaceutical industries [1–3]. However, the reaction conditions are often harsh, the reagent mixtures are corrosive (including Br^- or Cl^-), and the reactions are frequently unselective. The reactions also generate environmentally hazardous waste and by-products [3]. Frequently, oxidation reactions of saturated hydrocarbons are

catalysed by dissolved salts of redox-active metals [4] or peroxides at high temperature and pressure, but environmental concerns provide a strong incentive to identify more benign catalytic reactions [2]. The rational use of appropriate semiconductors and the fine control of reaction conditions can promote organic reactions with high selectivity with the unique promising advantages of operating at room temperature and utilizing solar light as the energy source [5].

Selective cyclohexane oxidation to cyclohexanol and cyclohexanone is relatively important in the chemical industry. More than one billion tonnes of cyclohexanol and cyclohexanone are produced each year worldwide [6], and these compounds are important intermediates in the synthesis of adipic acid and ϵ -caprolactam, which are in turn ultimately used to manufacture nylon polymers [7–9]. An ideal procedure for the oxidation of cyclohexane would selectively yield cyclohexanol and cyclohexanone with 100% conversion

* Corresponding author at: Faculty of Chemical Sciences, University of Concepción, University Campus, Concepción, Chile.

E-mail address: dcontrer@udec.cl (D. Contreras).

using molecular oxygen as the oxidant under mild conditions (room temperature and atmospheric pressure) using a highly active catalyst. It has been reported that cyclohexanol and cyclohexanone can be formed in the liquid phase using photocatalysts with titanium dioxide at room temperature and pressure [7,10–12]. TiO₂ is especially suitable as a photocatalyst compared to other semiconductors because it is highly photo-reactive, cheap, non-toxic, chemically and biologically inert, and photostable [13,14].

Several authors have used photocatalyst-based systems for the selective oxidation of cyclohexane to cyclohexanol. Some of these papers are shown in Table 1. The best selectivity for cyclohexanol production in the liquid phase was attained by Boarini et al. [12] and Hattori et al [9], but the cyclohexane was included in the solvents (dichloromethane and acetonitrile, respectively). Sannino et al. [15] achieved the best cyclohexanol selectivity (CH_{one}/CH_{ol} ratio=0.20) using TiO₂ doped with Au at 0.5%. However, the reaction was performed in the gas phase at 373 K.

Most of the systems shown in Table 1 used TiO₂ as the catalyst and UV radiation because the high bandgap of TiO₂ (3.2 eV) implies that wavelengths below 387 nm promote electrons from the valence band to the conduction band. The inactivity of TiO₂ under visible light is considered the overriding limitation of this material [20]. Because less than 5% of the solar flux at the surface of the Earth lies in the UV region, many strategies have been developed to induce visible light photocatalytic activity in TiO₂ systems, including anion doping [21–25] and doping with traces of transition metals [26–31]. Among the anions used as doping elements, nitrogen has shown great potential to improve the visible light photocatalytic activity [32]. Among the transition metals used as doping elements, iron(III) seems to be most attractive because it is non-toxic and abundant in nature and because its ionic radius is similar to that of Ti(IV) [33–36].

To enable more efficient use of the solar spectrum, numerous efforts have focused on the development of new semiconductor materials for photocatalytic applications under visible light [37]. Hattori et al. [9] used a photocatalyst based on layered titanate (K_{0.7}Ti_{1.73}Li_{0.27}O₄ modified with FeO) activated by simulated solar radiation (under 550 nm). In addition, bismuth oxyhalides (BiOX, X=Cl, Br, I) have recently been used [38–40] because they show photocatalytic activity under visible light in addition to adequate chemical stability and electrical and optical properties.

Despite results in the literature about the selective photocatalytic oxidation of cyclohexane to cyclohexanol and the use of different photocatalysts activated with visible or solar light, no systematic study has described the different properties of TiO₂-based and BiOX-based photocatalysts in the selective oxidation of cyclohexane to cyclohexanol under visible radiation.

In this paper, a systematic study of the selective photooxidation of cyclohexane to cyclohexanol was performed using five TiO₂-based photocatalysts and three BIOX-based photocatalysts with visible radiation under ambient conditions. The ratio of the products was related to the physical properties of the photocatalyst and the radical intermediates that were identified.

2. Experimental

2.1. Catalyst synthesis

Iron(III) acetylacetone, titanium(IV) isopropoxide, ethanol, urea, bismuth(III) nitrate pentahydrate, iron(III) nitrate nonahydrate, potassium chloride, potassium bromide, potassium iodide, cyclohexane, cyclohexanol and cyclohexanone standards were purchased from Sigma-Aldrich, Merck and Productos Químicos Monterrey. All reagents and solvents were used as received without further purification.

Samples of mesoporous Fe-doped TiO₂ were prepared according to a modified synthetic procedure described by Qamar et al. [20]. In a typical synthesis procedure, 1.5 mL of titanium(IV) isopropoxide, Ti[OCH(CH₃)₂]₄, was added dropwise to 20 mL of ethanol, and then the required molar ratio of iron(III) acetylacetone, Fe(C₅H₇O₂)₃, was added. The resulting solution was stirred for 30 min. To perform controlled hydrolysis, 50 mL of 10% (v/v) acetic acid was added to the solution dropwise, and the resulting solution was stirred for an additional 1 h. Then, the flask was stirred over a hot plate at 100 °C until all solvents evaporated. The dried gel was crushed into a fine powder and dried at 70 °C for subsequent calcination at 450 °C for 24 h with a ramp rate of 10 °C/min in air.

N-doped mesoporous TiO₂ was prepared according to a synthetic procedure described by Zalas [41] as follows: 15 mL of Ti[OCH(CH₃)₂]₄ (Aldrich, 97%) was added to a magnetically stirred solution of 2 g of urea in 45 mL of absolute ethanol, followed by 0.5 mL of 65% nitric acid and 3 mL of distilled water. The mixture was transferred to a Teflon-lined stainless steel autoclave and maintained at 80 °C for 48 h. The obtained deposit was separated from the liquid residue via decantation and dried at 80 °C overnight. The yellow solid was milled in an agate mortar for subsequent calcination at 300 °C for 2 h.

Bismuth oxyhalides, BiOXs (X=Cl[−], Br[−], I[−]), were prepared according to a modified synthetic procedure described by Wang et al. [38]. Bi(NO₃)₃•5H₂O (10 mmol) was dissolved in 100 mL of 1.57 mol L^{−1} acetic acid solution to obtain solution A. Solution B was prepared by dissolving 10 mmol KXs (X=Cl, Br, I) in 100 mL of distilled water. Solution B was slowly added to solution A dropwise over 2 h to form a coloured precipitate. The pH of the suspension was adjusted to 10, and the resulting solution was stirred for 1 h at room temperature. Then, the suspension was filtered, washed with distilled water, and fully dried at 70 °C.

2.2. Catalyst characterization

X-ray diffraction (XRD) patterns of the solid products were collected using a Bruker D8 Advance X-ray diffractometer using Cu K_α radiation as the source with a working voltage and current of 40 kV and 30 mA, respectively. The intensity of the diffraction peaks was recorded in the 10–80° (2θ) range in increments of 0.05° with a counting time of 0.5 s per step. The crystallite sizes of the semiconductor photocatalyst samples were estimated using the Debye–Scherrer formula (Eq. (1)), where D is the average crystallite size, K is a dimensionless shape factor (in this case, with a value of 0.94), λ is the X ray radiation wavelength (Cu K_α=0.154056 nm), β is the band broadening at half the maximum intensity (FWHM), and θ is the diffraction angle.

$$D = \frac{K\lambda}{\beta \cos \theta} \quad (1)$$

UV-vis diffuse reflectance spectra were recorded with an Agilent Cary 5000 UV/Vis/NIR spectrophotometer. The bandgap of the semiconductor photocatalyst was determined from a Tauc plot obtained from the UV-vis diffuse reflectance spectra. The relational expression proposed by Tauc, Davis, and Mott [42,43] (Eq. (2)) was used.

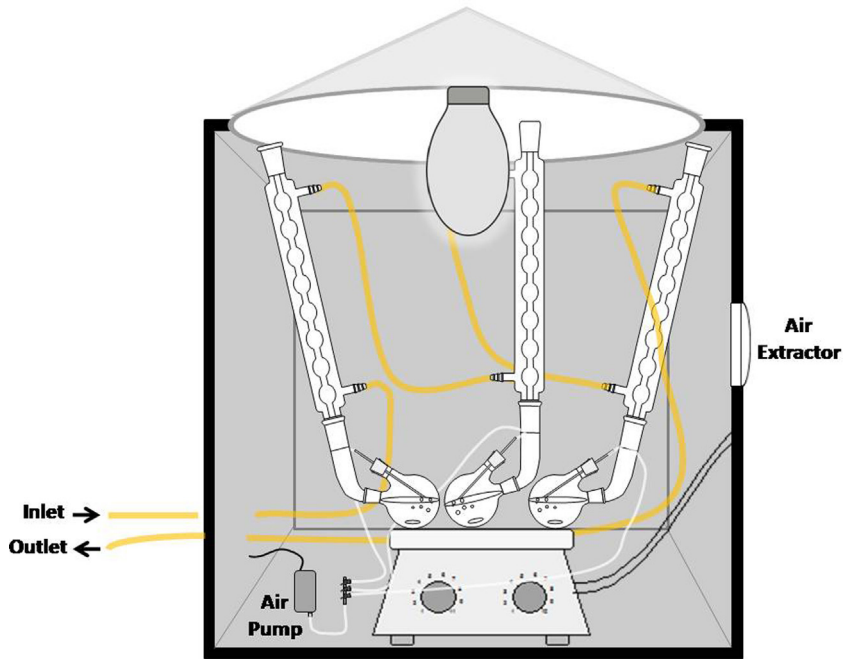
$$h\nu\alpha^{1/n} = A(h\nu - E_g) \quad (2)$$

h is Planck's constant, ν is the vibration frequency, α is the absorption coefficient, E_g is the bandgap, and A is a proportional constant. The value of the exponent n denotes the nature of the simple transition. For an indirect allowed transition, n=2. The α in the Tauc equation is substituted with the Kubelka–Munk function, F(R_∞). The crystal morphology of the products was observed by scanning electron microscopy (FEI–Nova NanoSEM 200). Nitrogen adsorp-

Table 1

Summary of studies on the selective photocatalytic oxidation of cyclohexane over different photocatalysts.

Reference	Catalyst	Illumination source	Experimental conditions	Time (h)	Chone/CHol ratio ^a
[10]	TiO ₂ (Pt doped)/0.7 g dm ⁻³	HP Hg (>250)	Air bubbling	6	17.2
[12]	TiO ₂ (P25)/4 g dm ⁻³	MP Hg (>360)	C ₆ H ₆ :CH ₂ Cl ₂ = 1:1 PO ₂ = 3.3 kPa	4	0.77
[15]	TiO ₂ (P25)/55 g dm ⁻³	LP Hg (>365)	C ₆ H ₆ :H ₂ O = 1:8, H ₂ O ₂ = 1.6 mol dm ⁻³ , O ₂ bubbling	2	1.46
[7]	TiO ₂ (P25)/1 g dm ⁻³	Xe (>225)	O ₂ bubbling	0.75	8.35
[16]	TiO ₂ (P25)/1 g dm ⁻³	MP Hg (>360)	Air bubbling	4.3	2.67
[17]	TiO ₂ (P25)/2 g dm ⁻³	Monochromatic radiation (=303)	C ₆ H ₆ :CH ₂ Cl ₂ = 1:1, air saturated before reaction start	0.75	1.34
[18]	TiO ₂ (anatase)/1 g dm ⁻³	HP Hg (>250)	Humidified air bubbling	5.7	4
[9]	Layered titanate (K _{0.7} Ti _{1.73} Li _{0.27} O ₄) modified 0.13% FeO/1.5 g dm ⁻³	Solar simulator (>350)	C ₆ H ₆ :CH ₃ CN = 1:9 O ₂ saturated before reaction start	6	0.89
[19]	TiO ₂ (0.5% Au doped)/1.2 g (20 g glass spheres)	UVA LED (=365)	C ₆ H ₆ :O ₂ = 1:3, gas phase (He stream) at 373 K	1.8	0.20

^a Cyclohexanone/cyclohexanol ratio.**Fig. 1.** Scheme of the photocatalytic reactor.

tion isotherms at -196°C were obtained using a BELSORP-mini II surface area and a pore size analyser.

2.3. Cyclohexane oxofunctionalization

The oxofunctionalization of 25 mL of cyclohexane was performed in a 50-mL 2-neck round-bottom flask fitted with a reflux condenser in the presence of 25 mg of catalyst (1 mg/mL) and 25 μL of nanopure water (Fig. 1). For each reaction, the system was saturated with 1 atm of air during the reaction time (3 h). Photocatalytic oxidation reactions were carried out under visible radiation generated by a 400 W metal halide lamp (Osram Powerstar HQI-E 400 W/D Pro Daylight). The emission spectrum of the lamp (Fig. 2) was recorded with a fluorescence spectrometer (LS-45, Perkin Elmer) in luminescence mode. The temperatures inside the photocatalytic reactor reached $37 \pm 2^{\circ}\text{C}$.

To identify the compounds obtained from the photocatalytic oxidation of cyclohexane, a 1.0 μL aliquot was removed from the reaction mixture and injected into a GC-MS system. GC-MS

analysis was performed on a 5890 Series II gas chromatograph (Hewlett Packard Corporation, Palo Alto, California, USA) interfaced with a 5972 Mass Selective Detector Quadrupole (Hewlett Packard Corporation, Palo Alto, California, USA). The analytes were separated in a crosslinked 5% diphenyl–95% dimethylsiloxane column (Hewlett Packard Corporation, Palo Alto, California, USA). The temperature programme was an isotherm at 40°C for 15 min. Helium was used as the carrier gas at a constant flow of 1 mL/min, and data acquisition was performed in electron impact ionization (EI) mode. The temperature inlet was set to 250°C , and the source was set to 280°C .

CO_2 produced in the photocatalytic oxidation of cyclohexane was determined by precipitation in $\text{Ba}(\text{OH})_2$. For this determination the reactor outlet was coupled to a CO_2 trapping system, where the gas produced in the reaction is bubbled into a test tube with $\text{Ba}(\text{OH})_2$ 0.1 mol L⁻¹. The tube, capped with a rubber stopper, had a glass tube inlet which extended inside until the bottom of the test tube. To release the air, the rubber stopper was later perforated with a hollow needle. In this system, all the CO_2 is precipitated as BaCO_3 .

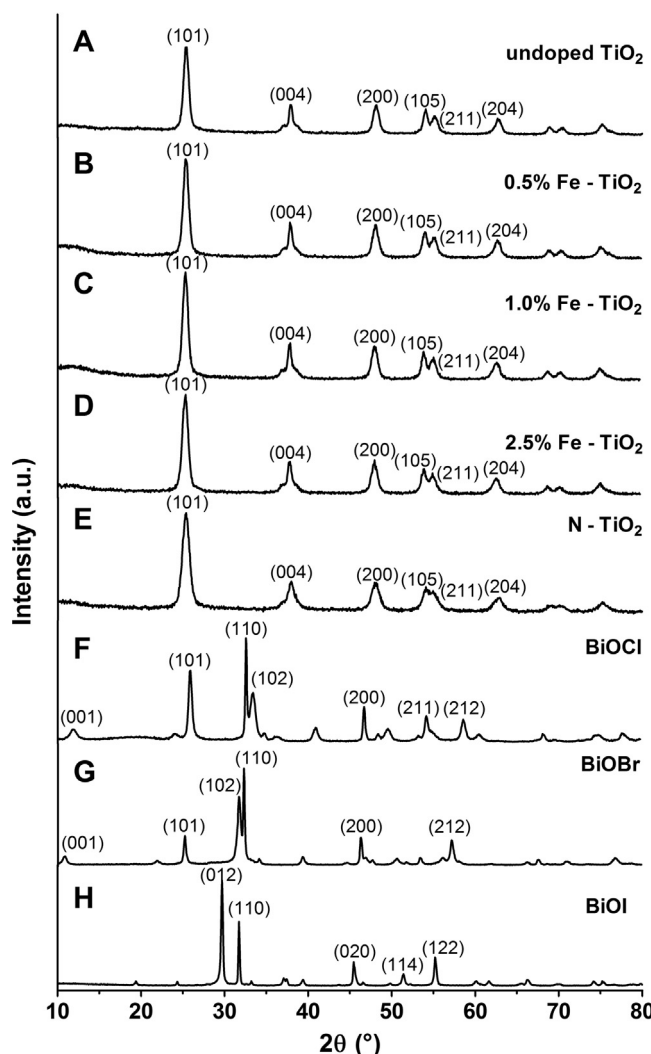


Fig. 2. Powder XRD patterns of (A) TiO_2 , (B) 0.5% Fe- TiO_2 , (C) 1.0% Fe- TiO_2 , (D) 2.5% Fe- TiO_2 , (E) N- TiO_2 , (F) BiOCl, (G) BiOBr and (H) BiOI.

[44,45], which amount is later quantified by turbidimetry [46] using a Hach turbidimeter (2100Q portable turbidimeter). The analytic method was validated by using a calibration curve with BaCO_3 . The CO_2 concentration was determined from this calibration curve. CO_2 free air injected in the reactor at the beginning of the experiment was supplemented by using a double $\text{Ba}(\text{OH})_2$ trap.

2.4. In situ Electron Paramagnetic Resonance Experiments

To investigate the formation of radical species during the oxidation of cyclohexane over the photoactivated surface of the

photocatalysts, *in situ* Electron Paramagnetic Resonance (EPR) measurements were performed with an EMX micro 6/1 Bruker ESR spectrometer working at X-band equipped with a Bruker Super High QE cavity resonator using N-*tert*-butyl- α -phenylnitron (PBN) as a spin trap for this apolar system. A 1-mg quantity of each photocatalyst was dispersed in 1 mL of cyclohexane containing 10 mmol L⁻¹ of PBN and 0.1% (v/v) nanopure water. The reaction was initiated by turning on the irradiation source. The reaction system was saturated with air during the reaction time. The reaction was carried out in an EPR sample tube (ER 221TUB/, 4 mm I.D.) inside the EPR cavity irradiated with the metal halide lamp described above.

The *in situ* measurement was performed at room temperature. Typical instrumental conditions were as follows: centre field, 3514 G; sweep width, 200 G; microwave power, 20 dB; modulation frequency, 100 kHz; time constant, 0.01 ms; sweep time, 30 s; modulation amplitude, 1.00 G; and receiver gain, 30 dB.

3. Results and discussion

3.1. Catalyst characterization

The structural and electronic properties of the synthesized semiconductor photocatalysts are presented in Table 2, and the XRD patterns are shown in Fig. 2. The XRD patterns of samples of TiO_2 , N-doped TiO_2 , and Fe-doped TiO_2 were indexed to the anatase phase of TiO_2 (JCPDS Card No. 4–477). The diffraction patterns of BiOCl, BiOBr and BiOI were indexed to the tetragonal phase of BiOCl (JCPDS Card No. 6–249), tetragonal phase of BiOBr (JCPDS Card No. 78–348) and tetragonal phase of BiOI (JCPDS Card No. 73–2062), respectively.

The diffraction patterns of BiOI showed an intense signal at 31.7° (20) assigned to the (1 1 0) facet. Pan et al. [47] reported that a BiOI catalyst with an exposed (1 1 0) facet exhibited better catalytic activity than a BiOI catalyst with another type of exposed facets. They attributed this activity to the ability of the (1 1 0) facet to generate $\cdot\text{OH}$ radicals directly. Other authors have presented evidence suggesting that the exposure of the (1 1 0) facet contributes to effective heterojunction between the (1 1 0) and (0 0 1) facets. This effect inhibits the recombination of charge carriers [48]. However, it has been reported that the exposure of the (1 1 0) and (0 0 1) facets depends of the pH value for co-precipitation in the synthesis of BiOBr. In this work, the ratio (1 1 0)/(0 0 1) was 9.7 for BiOBr at a precipitation pH close to 10. This result is in agreement with the trend reported by Li et al. [49].

A plot of the transformed Kubelka–Munk function versus the energy of the light absorbed by the photocatalysts is shown in Fig. 3. A shift in the bandgap towards lower energies associated with an incremental amount of iron was observed (Table 2), similar to that reported by Qamar et al. [20]. This shift can be explained by the overlap of the Fe 3d, Ti 3d and O 2p states, which eventually induces the absorption of higher wavelength photons by TiO_2 [20]. On the

Table 2

Structural and electronic properties of the synthesized semiconductor photocatalysts.

Photocatalyst	Crystallite size ^a (nm)	BET surface area (m ² g ⁻¹)	Pore size (nm)	Pore volume (cm ³ g ⁻¹)	Bandgap ^b (eV)
TiO_2	11.20	129.54	9.26	0.3015	3.16
0.5% Fe- TiO_2	11.50	137.84	9.26	0.2944	3.01
1.0% Fe- TiO_2	11.50	132.92	9.26	0.3039	3.00
2.5% Fe- TiO_2	10.64	141.98	9.10	0.2806	2.73
N- TiO_2	9.05	173.41	9.10	0.2840	3.15
BiOCl	42.20	22.26	20.80	0.1157	3.50
BiOBr	36.79	16.24	26.80	0.1088	2.90
BiOI	34.36	4.56	27.80	0.0317	1.83

^a Calculated from XRD measurements using the Scherrer equation.

^b Calculated from diffuse reflectance UV-vis spectra using the Kubelka–Munk function.

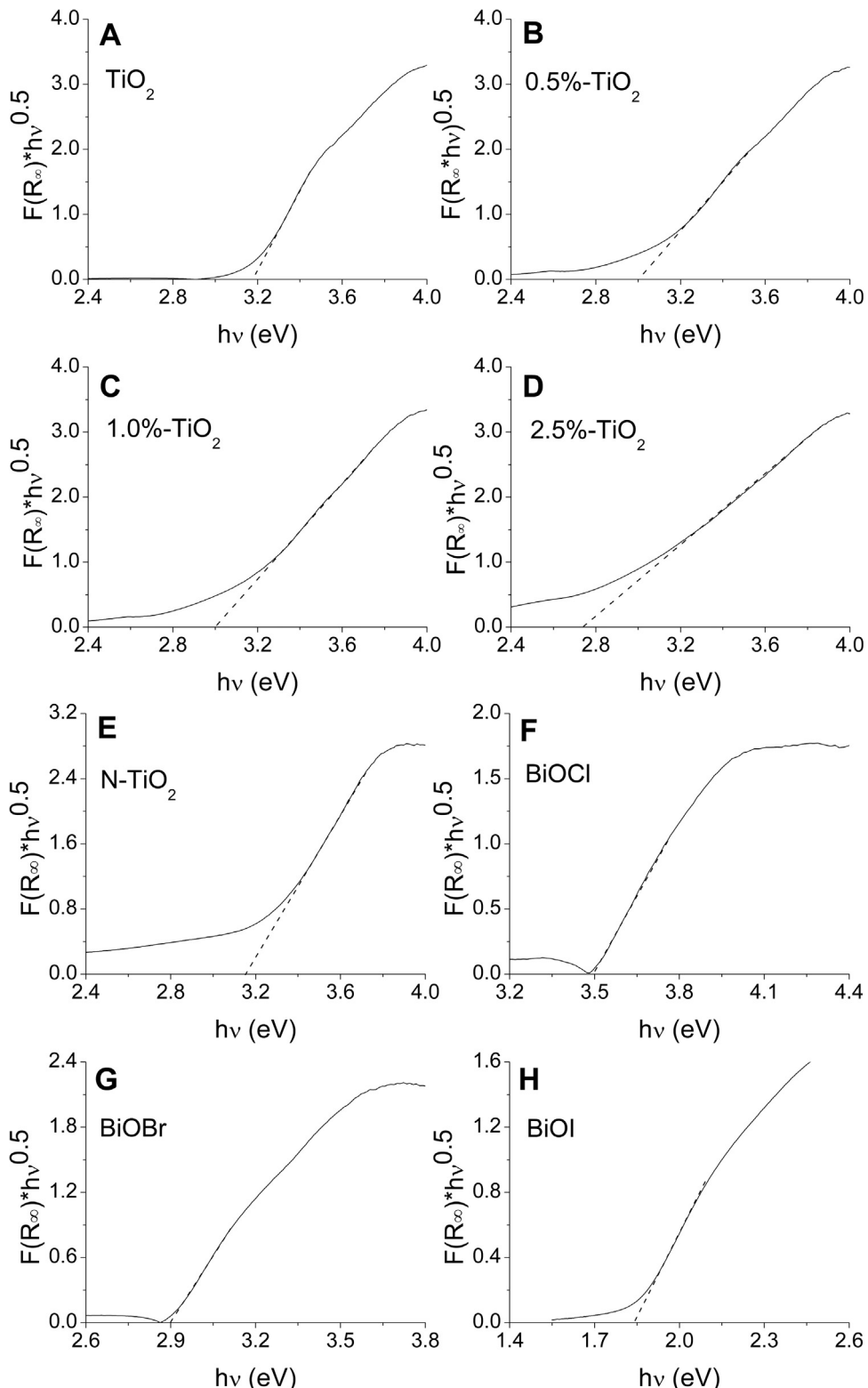


Fig. 3. Optical bandgaps of (A) TiO_2 , (B) 0.5% Fe- TiO_2 , (C) 1.0% Fe- TiO_2 , (D) 2.5% Fe- TiO_2 , (E) N- TiO_2 , (F) BiOCl, (G) BiOBr and (H) BiOI.

other hand, in the bismuth oxyhalides the bandgap decreases, as the atomic number of halogen increases. The adsorption and desorption isothermal curves of the TiO_2 , 0.5% Fe- TiO_2 , 1.0% Fe- TiO_2 , 2.5% Fe- TiO_2 , and N- TiO_2 samples (Fig. 4A, B, C, D and 4, respectively) were classical type IV and contained hysteresis, suggesting a mesoporous presence [50]. The BiOCl, BiOBr and BiOI samples (Fig. 4F, G and H, respectively) presented type II adsorption and

desorption isotherms, suggesting a non-porous presence or possibly macroporous materials [51]. The undoped TiO_2 sample (Fig. 5A) presented particles of approximately 11 and 15 nm in diameter, whereas the 0.5% Fe- TiO_2 and 1.0% Fe- TiO_2 samples (Fig. 5B and C, respectively) presented particles of approximately 9 and 12 nm in diameter. By contrast, the sample of 2.5% Fe- TiO_2 (Fig. 5D) presented smaller particles sizes of approximately 7–8 nm. These

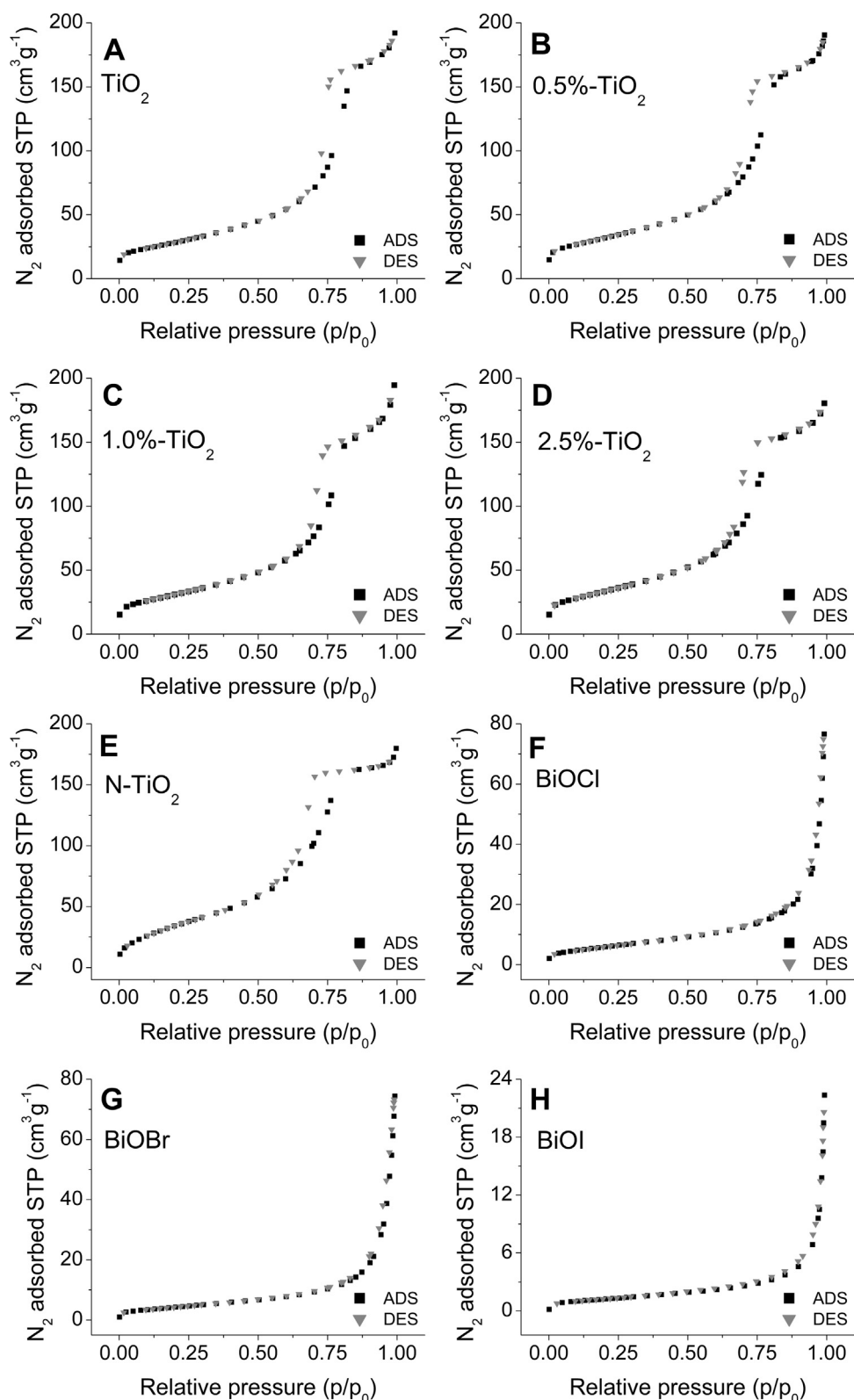


Fig. 4. Adsorption–desorption isotherms at 77 K of (A) TiO₂, (B) 0.5% Fe–TiO₂, (C) 1.0% Fe–TiO₂, (D) 2.5% Fe–TiO₂, (E) N–TiO₂, (F) BiOCl, (G) BiOBr and (H) BiOI.

results are in agreement with the superficial areas calculated from the N₂ adsorption–desorption isotherms, which showed a trend of increasing area as a function of the amount of iron as dopant. The N–TiO₂ (Fig. 5E) sample presented particles of approximately 8–10 nm in diameter. This result is in agreement with the particles

size estimated from the Scherrer equation of 9.05 nm. SEM images of BiOX revealed nanosheets with a thickness of approximately 5 nm. BiOCl (Fig. 5F) showed an irregular laminar structure. The BiOBr and BiOI samples presented a hierarchical three-dimensional flower-like structure (Fig. 5G and H, respectively).

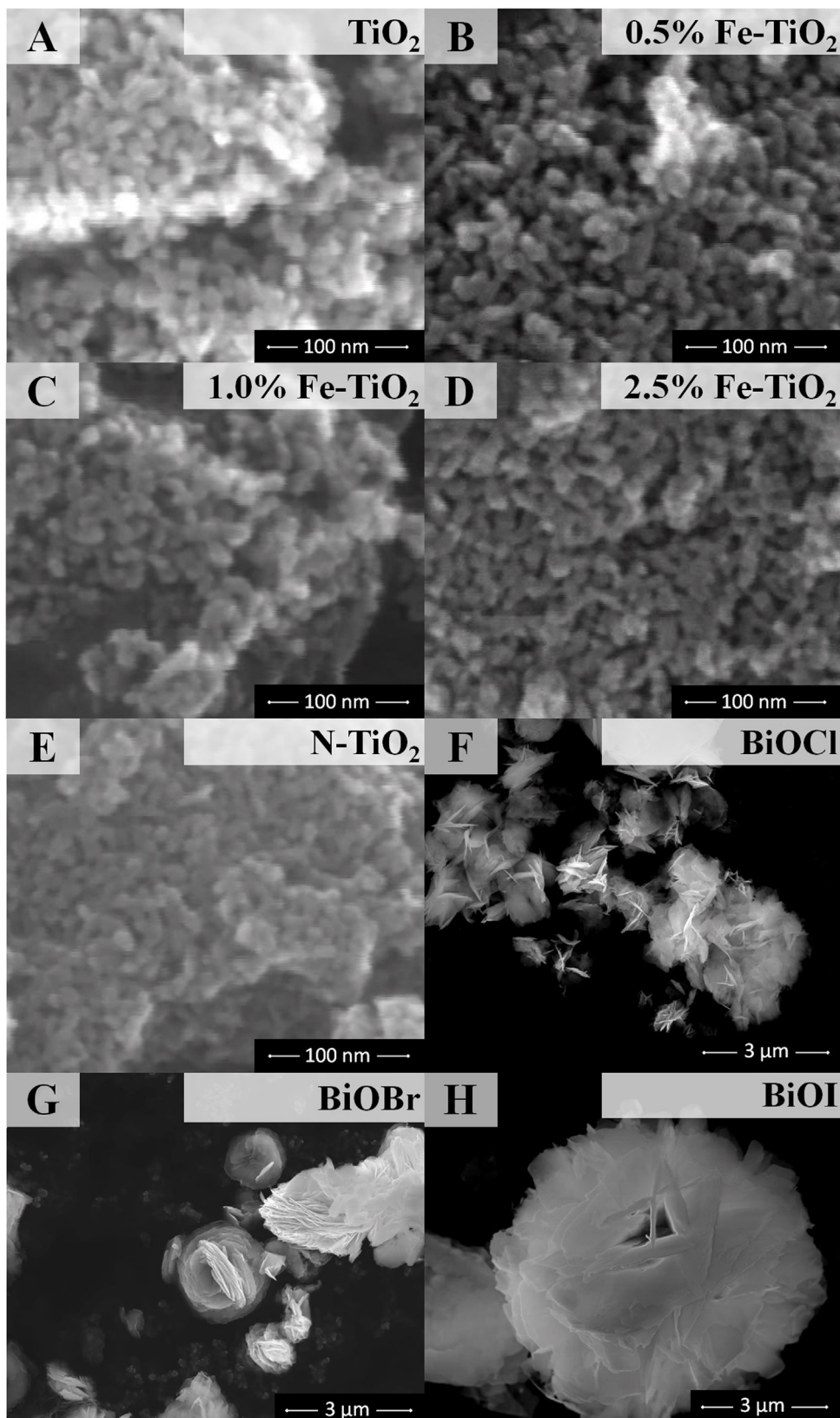


Fig. 5. SEM micrographs of (A) TiO_2 , (B) 0.5% Fe- TiO_2 , (C) 1.0% Fe- TiO_2 , (D) 2.5% Fe- TiO_2 , (E) N- TiO_2 , (F) BiOCl, (G) BiOBr and (H) BiOI.

3.2. Cyclohexane oxofunctionalization

After a reaction time of 180 min, only the products cyclohexanol, cyclohexanone and CO_2 were detected in all photocatalytic

systems assayed. The cyclohexanol, cyclohexanone and CO_2 were quantified, and the selectivity of the photocatalyst for cyclohexanol or cyclohexanone was related to the cyclohexanone/cyclohexanol ratio (CHone/CHol). The yields for cyclohexanol, cyclohexanone

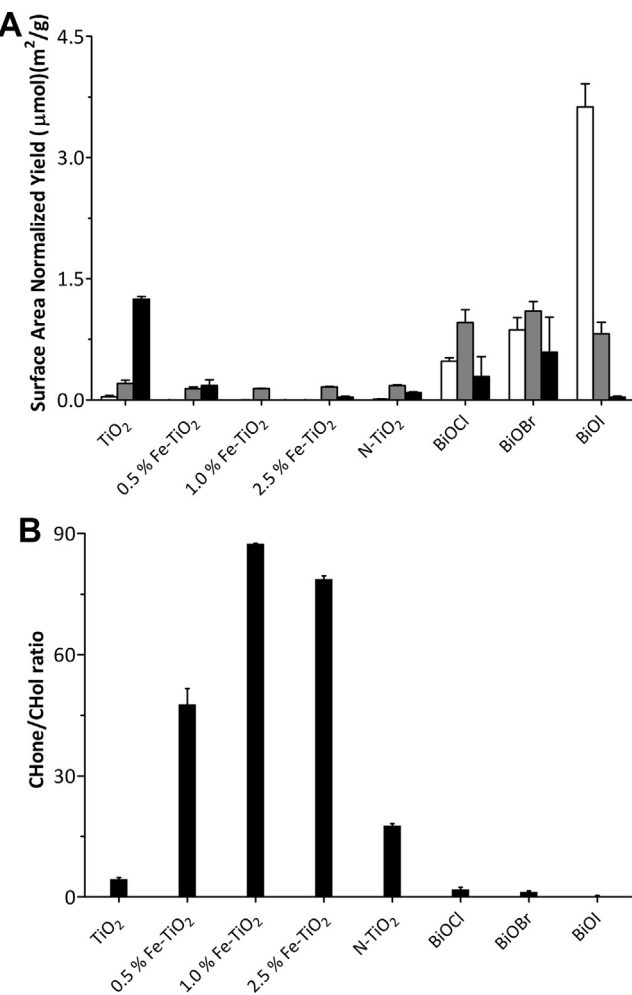


Fig. 6. A. The surface area normalized yield of cyclohexane oxofunctionalization under visible light irradiation. White and gray columns represent cyclohexanol and cyclohexanone yield, respectively. Black columns represent carbon dioxide yield, determined by turbidimetry. B. Cyclohexanone/cyclohexanol ratio attained in the different photocatalytic systems.

and CO₂ were normalized by surface area (bar plots in Fig. 6). The maximum normalized yield for cyclohexanol was attained by the BiOI photocatalyst ($3.6 \pm 0.3 \mu\text{mol m}^{-2} \text{ g}$), and the maximum normalized yield for cyclohexanone was reached by the BiOBr photocatalyst ($1.1 \pm 0.1 \mu\text{mol m}^{-2} \text{ g}$). The highest normalized yields were achieved by the BiOX photocatalyst, especially on cyclohexanol (Fig. 6A).

The maximum normalized yield of carbon dioxide was attained by the TiO₂ ($1.20 \pm 0.03 \mu\text{mol m}^{-2} \text{ g}$). The CO₂ yield of Fe-doped TiO₂ and the N-doped TiO₂ was lower than that of undoped TiO₂, indicating a negative effect of iron and nitrogen doping on the photocatalytic performance of TiO₂-based photocatalysts. CO₂ production in oxofunctionalization reactions of cyclohexane photocatalysed by bismuth oxyhalides was observed. Nevertheless, the yield of CO₂ was lower than cyclohexanol and cyclohexanone. On the other hand, BiOI exhibit the lower normalized yield of CO₂ of bismuth oxyhalides ($3.3 \times 10^{-2} \pm 1.6 \times 10^{-2} \mu\text{mol m}^{-2} \text{ g}$). This result is in agreement with the higher selectivity of this photocatalyst to cyclohexanol.

Important differences in the CHone/CHol ratio were observed for the photocatalytic systems that were assayed (Fig. 6B). Thus, higher CHone/CHol ratios were attained by the TiO₂-based photocatalyst (more selective for cyclohexanone). The most selective photocatalyst for cyclohexanone was 1.0% Fe-TiO₂ (CHone/CHol

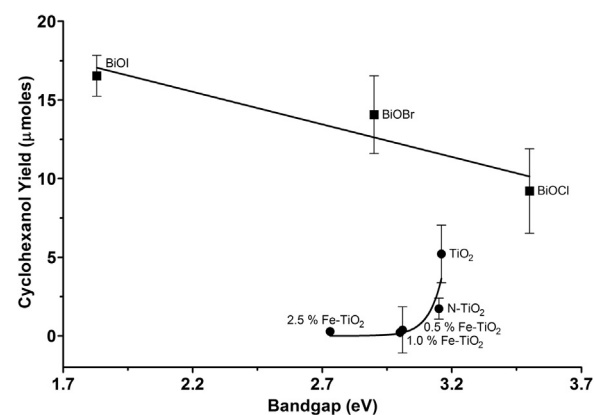


Fig. 7. Dependence of the cyclohexanol yield on the bandgap for the photocatalysts. The circles represent a TiO₂-based photocatalyst, and the squares represent BiOX.

ratio = 87.50 ± 0.02). Lower CHone/CHol ratios were realized by the BiOX photocatalysts (more selective for cyclohexanol). Among these, BiOI showed the highest selectivity for cyclohexanol (CHone/CHol ratio = 0.23 ± 0.19).

The CHone/CHol ratios and yields depended on the physical properties of the photocatalysts that were studied. In this analysis, only a relationship between bandgap and cyclohexanol yield was observed (Fig. 7). Thus, the titanium dioxide-based photocatalyst and BiOXs exhibited different behaviours with respect to the conversion yield of cyclohexane to cyclohexanol. The TiO₂-based photocatalysts showed an exponential dependence ($r = 0.89$) of the cyclohexanol yield on the bandgap. These observations may be explained by decrease in the bandgap of TiO₂-based materials upon doping with iron or nitrogen (Table 2). The bathochromic shift in the bandgap of TiO₂ improves the efficiency of the photocatalysts due to the absorption of higher-wavelength photons, which further promotes cyclohexane oxidation to cyclohexanol. By contrast, for BiOX photocatalysts, the cyclohexanol yield depended linearly on the bandgap ($r = -0.94$).

To determine the differences between the selectivities shown by the TiO₂-based and the BiOX photocatalysts, the radical intermediates in the photocatalytic reaction were determined.

3.3. In situ electron paramagnetic resonance

The radical intermediates that formed during the photocatalytic oxidation of cyclohexane were detected by EPR spectroscopy using PBN as a spin trap. Fig. 8 shows the EPR spectra of the radical-PBN adduct that was formed in the photocatalytic oxidation reactions of cyclohexane using different photocatalysts. In all systems (except BiOI as the photocatalyst), only one triplet signal ($a^N = 13.6 \text{ G}$) was observed. This signal was assigned as cyclohexyloxy ($\text{C}_6\text{H}_{11}\text{O}\bullet$) according to the literature [18,52,53]. It has been reported that the spin trap of organic peroxy radicals at room temperature produces alkoxy radicals adducts rather than peroxy radical adducts [54–58].

Conte et al. [59] reported that the first step in the oxidation of hydrocarbons over a TiO₂-based photocatalyst is hydrogen abstraction, which produces an acyl radical. Thus, the oxidation of cyclohexane by the assayed photocatalyst produces cyclohexyl radicals (Eq. (3)). Under air-saturated conditions, these radicals react with oxygen, producing cyclohexylperoxy radicals (Eq. (4)). This radical, through recombination, produces cyclohexanol and cyclohexanone (Eq. (5)). This reaction pathway has been proposed in the literature for the oxidation of cyclohexane by a TiO₂-based photocatalysts [7,17,18] and should be the main pathway for the

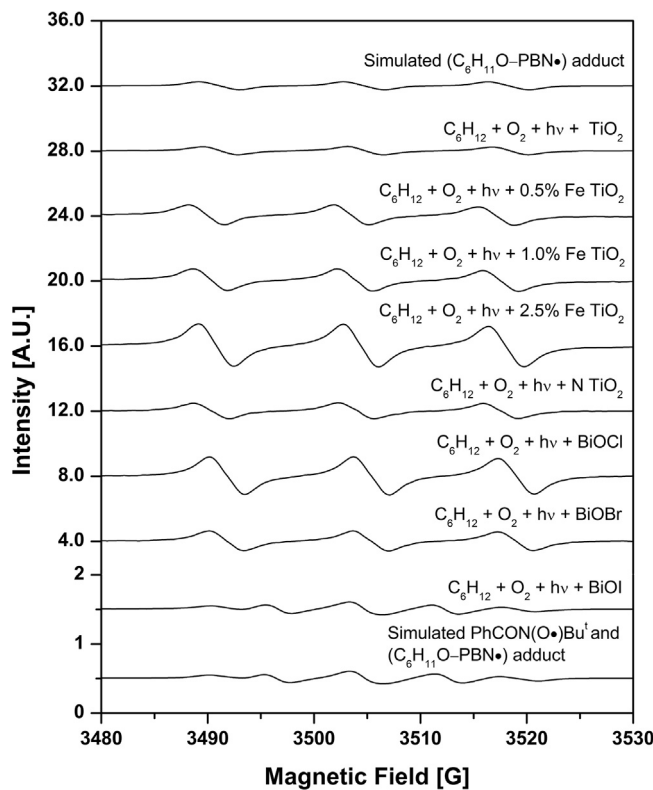
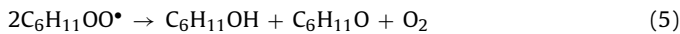


Fig. 8. EPR spectra obtained 650 s after photocatalytic oxofunctionalization of cyclohexane saturated with air under visible light irradiation by a 400 W metallic halide lamp.

production of cyclohexanol and cyclohexanone from the photocatalytic oxidation of cyclohexane.



The oxidation of cyclohexane photocatalysed by BiOI shows two EPR signals. These signals were identified as two partially overlapped triplets with hyperfine coupling constants of 13.6 G and 8.1 G. The first signal was assigned to $\text{C}_6\text{H}_{11}\text{O}\cdot$. The second signal was assigned to the $\text{PhCON(O}\cdot\text{)Bu}^\ddagger$ adduct (Fig. 8), which is an oxidation product from PBN. Its formation was evidence of the $\cdot\text{OH}$ radical [53].

The production of the $\cdot\text{OH}$ radical by a BiOI photocatalyst could be related to the higher yield and selectivity for cyclohexanol production (Fig. 6). Therefore, it is possible to propose that the most important route of cyclohexane oxidation through cyclohexanol photocatalysed by BiOI is through the $\cdot\text{OH}$ radical (Eq. (6)).



The BiOI photocatalyst shows a lower bandgap ($\lambda \leq 678$ nm). This value is on the edge of the emission region of the metal halide lamp (340 nm to 670 nm). The low radiation intensity could be related to the production of the $\cdot\text{OH}$ radical. To assess this effect, a new experiment was performed using an infrared lamp ranging from 550 nm to 780 nm with a maximum emission at 625 nm (Fig.S1). Under this condition, the $\text{PhCON(O}\cdot\text{)}$ adduct was observed (Fig.S2). Accordingly, the $\cdot\text{OH}$ radical did not depend on the intensity of the radiation but rather on the properties of the BiOI photocatalyst. As discussed above, the BiOI photocatalyst shows an intense DRX signal assigned to the (1 1 0) facet. Pan et al. [47] associated this facet directly with the production of $\cdot\text{OH}$ for BiOI.

This effect has not been reported in the literature for BiOCl and BiOBr.

3.4. Proposed pathway for cyclohexane oxidation

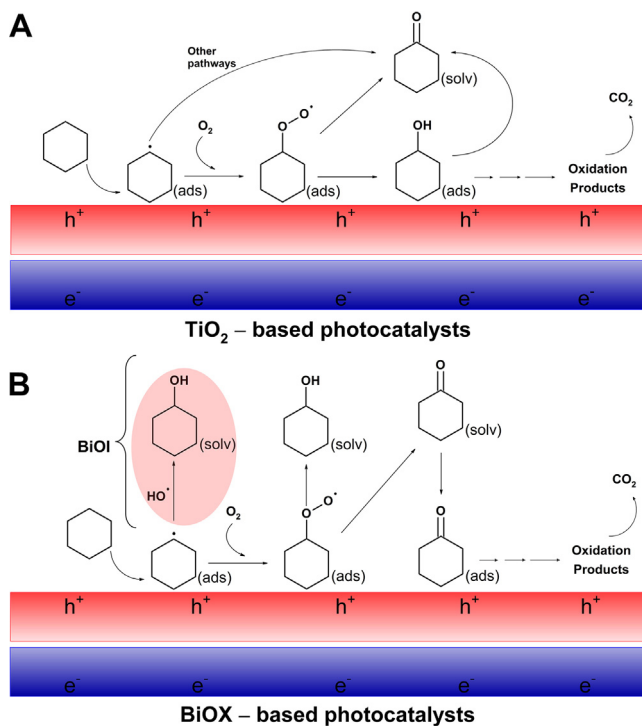
Based on the results discussed above, different pathways are proposed for the oxidation of cyclohexane using the TiO_2 or BiOX photocatalysts (Scheme I).

For all studied photocatalysts, in the first stage, H^\bullet abstraction by the photohole gives $\text{C}_6\text{H}_{11}\cdot$. Then, this radical reacts with oxygen to give $\text{C}_6\text{H}_{11}\text{OO}\cdot$. This compound disproportionates to $\text{C}_6\text{H}_{11}\text{OH}$ and $\text{C}_6\text{H}_{10}\text{O}$. In this stage, there are differences between the oxidation pathways of the photocatalysts. The TiO_2 -based photocatalyst (Scheme I-A) shows higher polarity than the BiOX photocatalysts. For the first materials, $\text{C}_6\text{H}_{11}\text{OH}$ should continue to be adsorbed on surface (hydrogen bonding and other van der Waals forces are established). The adsorbed $\text{C}_6\text{H}_{11}\text{OH}$ is further oxidized to $\text{C}_6\text{H}_{10}\text{O}$, resulting in low levels of $\text{C}_6\text{H}_{11}\text{OH}$ that decrease as the photocatalyst becomes more active. Moreover, other pathways for the formation of cyclohexanone from cyclohexane have been described, such as the reaction between the cyclohexyl radical and superoxide radical anion or perhydroxyl radical [12]. By contrast, the BiOX photocatalysts have lower surface polarity. Consequently, the $\text{C}_6\text{H}_{11}\text{OH}$ formed should be desorbed to the solution.

Similar amounts of both $\text{C}_6\text{H}_{11}\text{OH}$ and $\text{C}_6\text{H}_{10}\text{O}$ were detected when the oxidation was performed by BiOCl or BiOBr because the principal pathway is the disproportionation reaction of $\text{C}_6\text{H}_{11}\text{OO}\cdot$, which generates the same amounts of both compounds. Moreover, the amount of $\text{C}_6\text{H}_{11}\text{OH}$ is highest when the photocatalyst is BiOI (Scheme I-B). This effect could be explained by the production of the $\cdot\text{OH}$ radical (highlighted zone in Scheme I-B).

In TiO_2 photocatalysts cyclohexane is adsorbed on the photocatalyst surface, here is oxidized to cyclohexanol, which remains adsorbed and may be overoxidized to carboxylic acid and other short chain compounds not detectable by GC-MS. These oxidized products can further oxidized to CO_2 . The production of CO_2 depending on the photocatalyst is shown in Fig. 6A. Apparently there is no competition in the production of cyclohexanone and CO_2 , because both products have a common precursor, cyclohexylperoxyl radical. The cyclohexanol is oxidized to CO_2 because remains adsorbed on the photocatalysts surface through hydrogen bonding. In TiO_2 photocatalysts the more exposed facet is the (1 0 1) (Fig. 2), which has a high oxygen atoms density. This mean they have an oxygen rich surface, available to establish hydrogen bonding with more affinity for cyclohexanol than cyclohexanone. This could be a possible explanation to the lower amount of cyclohexanol and high amount of CO_2 attained by these systems. Of course, more experiments are necessary to confirm these assumptions.

On the other hand, in the BiOX based photocatalysts the cyclohexane should be oxidized to cyclohexylperoxyl radical. From this radical, cyclohexanol and cyclohexanone are produced. These compounds are released to the solution bulk. After that, cyclohexanone is adsorbed by the photocatalyst more efficiently than the cyclohexanol, because of the lower oxygen atoms density of BiOX surfaces, regarding TiO_2 based photocatalysts, to establish hydrogen bonding. In BiOX the facet is (1 1 0) is one of the most exposed facet (Fig. 2). Wherein, the oxygen atoms available to form hydrogen bonding should be lower than those available in anatase TiO_2 (1 0 1) facet. This could be the reason, because the amount of cyclohexanol is higher in the BiOX photocatalysts than the TiO_2 based photocatalysts. In these systems, other compounds different than cyclohexanol and cyclohexanone were not detected by GC-MS. Although, the formation of carboxylic acids and short chain com-



Scheme 1. Proposed pathways for cyclohexane oxidation over A. TiO_2 -based and B. BiOX photocatalysts.

ound is necessary for the production of CO_2 . The detection of such compounds is a problem that need further research.

Finally, the BiOI have an extra pathway for cyclohexanol generation, highlighted area in Scheme 1. In this way, a lower amount of cyclohexanone is formed, hence, a lower amount of cyclohexanone is adsorbed from the bulk solution.

4. Conclusions

The BiOX photocatalysts showed the highest selectivity for the production of cyclohexanol. By contrast, the TiO_2 -based photocatalysts showed the best yield for cyclohexanone production. For these photocatalysts, in all assayed systems, the cyclohexyloxy radical was identified as an intermediate. However, only when BiOI was utilized was there evidence of $\cdot\text{OH}$ radical production. A higher yield of cyclohexanol than cyclohexanone was obtained only when BiOI was used. The selectivity was associated with the differences in the properties of the photocatalyst surfaces between the BiOX photocatalysts and the TiO_2 -based photocatalysts. The special selectivity exhibited by BiOI was associated with $\cdot\text{OH}$ radical production.

Acknowledgements

The financial support for this work was granted by CONICYT National Doctoral Fellowship 21130450; The Pacific Alliance's student and academic mobility platform; FONDECYT 1160100 and FONDAP Solar Energy Research Center, SERC-Chile 15110019.

Appendix A. Supplementary data

Supplementary data associated with this article can be found, in the online version, at <http://dx.doi.org/10.1016/j.apcatb.2017.01.022>.

References

- [1] L. Barrio, P. Toribio, J. Campos-Martin, J. Fierro, An experimental and theoretical study of the catalytic effect of quaternary ammonium salts on the oxidation of hydrocarbons, *Tetrahedron* 60 (2004) 11527–11532.
- [2] E. Roduner, W. Kain, B. Sarkar, V. Urlacher, J. Pleiss, R. Glaser, W. Einicke, G. Sprenger, U. Beifuss, E. Klemm, C. Liebner, H. Hieronymus, S. Hsu, B. Pletker, S. Laschat, Selective catalytic oxidation of C-H bonds with molecular oxygen, *Chemcatchem* 5 (2013) 82–112.
- [3] M. Qadir, J. Scholten, J. Dupont, TiO_2 nanomaterials: highly active catalysts for the oxidation of hydrocarbons, *J. Mol. Catal. A Chem.* 383 (2014) 225–230.
- [4] R. Sheldon, *Metal-Catalyzed Oxidations of Organic Compounds: Mechanistic Principles and Synthetic Methodology Including Biochemical Processes*, Elsevier Science, 2012.
- [5] Y. Zhang, N. Zhang, Z. Tang, Y. Xu, Transforming CdS into an efficient visible light photocatalyst for selective oxidation of saturated primary C-H bonds under ambient conditions, *Chem. Sci.* 3 (2012) 2812–2822.
- [6] B. Retcher, J. Costa, J. Tang, R. Hage, P. Gamez, J. Reedijk, Unexpected high oxidation of cyclohexane by Fe salts and dihydrogen peroxide in acetonitrile, *J. Mol. Catal. A Chem.* 286 (2008) 1–5.
- [7] C. Almquist, P. Biswas, The photo-oxidation of cyclohexane on titanium dioxide: an investigation of competitive adsorption and its effects on product formation and selectivity, *Appl. Catal. A Gen.* 214 (2001) 259–271.
- [8] Y. Shiraishi, T. Hirai, Selective organic transformations on titanium oxide-based photocatalysts, *J. Photochem. Photobiol. C Photochem. Rev.* 9 (2008) 157–170.
- [9] H. Hattori, Y. Ide, S. Ogo, K. Inumaru, M. Sadakane, T. Sano, Efficient and selective photocatalytic cyclohexane oxidation on a layered titanate modified with iron oxide under sunlight and CO_2 atmosphere, *ACS Catal.* 2 (2012) 1910–1915.
- [10] W. Mu, J. Herrmann, P. Pichat, Room-temperature photocatalytic oxidation of liquid cyclohexane into cyclohexanone over neat and modified TiO_2 , *Catal. Lett.* 3 (1989) 73–84.
- [11] A. Sclafani, J. Herrmann, Comparison of the photoelectronic and photocatalytic activities of various anatase and rutile forms of titania in pure liquid organic phases and in aqueous solutions, *J. Phys. Chem.* 100 (1996) 13655–13661.
- [12] P. Boarini, V. Carassiti, A. Maldotti, R. Amadelli, Photocatalytic oxygenation of cyclohexane on titanium dioxide suspensions: effect of the solvent and of oxygen, *Langmuir* 14 (1998) 2080–2085.
- [13] J. Robertson, P. Robertson, L. Lawton, A comparison of the effectiveness of TiO_2 photocatalysis and UVA photolysis for the destruction of three pathogenic micro-organisms, *J. Photochem. Photobiol. A Chem.* 175 (2005) 51–56.
- [14] A. Mills, R. Davies, D. Worsley, Water – purification by semiconductor photocatalysis, *Chem. Soc. Rev.* 22 (1993) 417–425.
- [15] D. Sannino, V. Vaiano, P. Ciambelli, J. Murcia, M. Hidalgo, J. Navio, Gas-phase photocatalytic partial oxidation of cyclohexane to cyclohexanol and cyclohexanone on Au/TiO_2 photocatalysts, *J. Adv. Oxid. Technol.* 16 (2013) 71–82.
- [16] M. Gonzalez, S. Howell, S. Sikdar, Photocatalytic selective oxidation of hydrocarbons in the aqueous phase, *J. Catal.* 183 (1999) 159–162.
- [17] P. Du, J. Mouljin, G. Mul, Selective photo(catalytic)-oxidation of cyclohexane: effect of wavelength and TiO_2 structure on product yields, *J. Catal.* 238 (2006) 342–352.
- [18] M. Brusa, Y. Di Iorio, M. Churio, M. Grela, Photocatalytic air oxidation of cyclohexane in $\text{CH}_2\text{Cl}_2-\text{C}_6\text{H}_{12}$ mixtures over TiO_2 particles – an attempt to rationalize the positive effect of dichloromethane on the yields of valuable oxygenates, *J. Mol. Catal. A Chem.* 268 (2007) 29–35.
- [19] J. Carneiro, C. Yang, J. Mouljin, G. Mul, The effect of water on the performance of TiO_2 in photocatalytic selective alkane oxidation, *J. Catal.* 277 (2011) 129–133.
- [20] M. Qamar, B. Merzougui, D. Anjum, A. Hakeem, Z. Yamani, D. Bahnemann, Synthesis and photocatalytic activity of mesoporous nanocrystalline Fe-doped titanium dioxide, *Catal. Today* 230 (2014) 158–165.
- [21] R. Asahi, T. Morikawa, T. Ohwaki, K. Aoki, Y. Taga, Visible-light photocatalysis in nitrogen-doped titanium oxides, *Science* 293 (2001) 269–271.
- [22] S. Khan, M. Al-Shahry, W. Ingler, Efficient photochemical water splitting by a chemically modified N-TiO₂, *Science* 297 (2002) 2243–2245.
- [23] D. Mitoraj, H. Kisch, The nature of nitrogen-modified titanium dioxide photocatalysts active in visible light, *Angew. Chem. Int. Ed.* 47 (2008) 9975–9978.
- [24] W. Zhao, W. Ma, C. Chen, J. Zhao, Z. Shuai, Efficient degradation of toxic organic pollutants with $\text{Ni}_2\text{O}_3/\text{TiO}_2-\text{xBx}$ under visible irradiation, *J. Am. Chem. Soc.* 126 (2004) 4782–4783.
- [25] J. Shi, J. Chen, H. Cui, M. Fu, H. Luo, B. Xu, Z. Ye, One template approach to synthesize C-doped titania hollow spheres with high visible-light photocatalytic activity, *Chem. Eng. J.* 195 (2012) 226–232.
- [26] W. Choi, A. Termin, M. Hoffmann, The role of metal – ion dopants in quantum – sized TiO_2 – correlation between photoreactivity and charge – carrier recombination dynamics, *J. Phys. Chem.* 98 (1994) 13669–13679.
- [27] S. Kim, S. Hwang, W. Choi, Visible light active platinum-ion-doped TiO_2 photocatalyst, *J. Phys. Chem. B* 109 (2005) 24260–24267.
- [28] L. Peng, T. Xie, Y. Lu, H. Fan, D. Wang, Synthesis, photoelectric properties and photocatalytic activity of the $\text{Fe}_2\text{O}_3/\text{TiO}_2$ heterogeneous photocatalysts, *Phys. Chem. Chem. Phys.* 12 (2010) 8033–8041.

- [29] L. Devi, N. Kottam, B. Murthy, S. Kumar, Enhanced photocatalytic activity of transition metal ions Mn²⁺, Ni²⁺ and Zn²⁺ doped polycrystalline titania for the degradation of Aniline Blue under UV/solar light, *J. Mol. Catal. A Chem.* 328 (2010) 44–52.
- [30] J. Choi, H. Park, M. Hoffmann, Effects of single metal-ion doping on the visible-light photoreactivity of TiO₂, *J. Phys. Chem. C* 114 (2010) 783–792.
- [31] V. Binas, K. Sambani, T. Maggos, A. Katsanaki, G. Kiriacidis, Synthesis and photocatalytic activity of Mn-doped TiO₂ nanostructured powders under UV and visible light, *Appl. Catal. B Environ.* 113 (2012) 79–86.
- [32] J. Fu, Y. Tian, B. Chang, F. Xi, X. Dong, Soft-chemical synthesis of mesoporous nitrogen-modified titania with superior photocatalytic performance under visible light irradiation, *Chem. Eng. J.* 219 (2013) 155–161.
- [33] M. Litter, J. Navio, Photocatalytic properties of iron-doped titania semiconductors, *J. Photochem. Photobiol. A Chem.* 98 (1996) 171–181.
- [34] J. Navio, G. Colon, M. Litter, G. Bianco, Synthesis, characterization and photocatalytic properties of iron-doped titania semiconductors prepared from TiO₂ and iron(III) acetylacetone, *J. Mol. Catal. A Chem.* 106 (1996) 267–276.
- [35] J. Navio, J. Testa, P. Djedjeian, J. Padron, D. Rodriguez, M. Litter, Iron-doped titania powders prepared by a sol-gel method. Part II: photocatalytic properties, *Appl. Catal. A Gen.* 178 (1999) 191–203.
- [36] K.E. deKrafft, C. Wang, W. Lin, Metal-organic framework templated synthesis of Fe₂O₃/TiO₂ nanocomposite for hydrogen production, *Adv. Mater.* (2012) 2014–2018.
- [37] A. Martinez-de la Cruz, U. Garcia-Perez, S. Sepulveda-Guzman, Characterization of the visible-light-driven BiVO₄ photocatalyst synthesized via a polymer-assisted hydrothermal method, *Res. Chem. Intermed.* 39 (2013) 881–894.
- [38] S. Wang, L. Wang, W. Ma, D. Johnson, Y. Fang, M. Jia, Y. Huang, Moderate valence band of bismuth oxyhalides (BiOXs, X = Cl, Br, I) for the best photocatalytic degradation efficiency of MC-LR, *Chem. Eng. J.* 259 (2015) 410–416.
- [39] W. Zhang, Q. Zhang, F. Dong, Visible-light photocatalytic removal of NO in air over BiOX (X = Cl, Br, I) single-crystal nanoplates prepared at room temperature, *Ind. Eng. Chem. Res.* 52 (2013) 6740–6746.
- [40] X. Qin, H. Cheng, W. Wang, B. Huang, X. Zhang, Y. Dai, Three dimensional BiOX (XCl, Br and I) hierarchical architectures: facile ionic liquid-assisted solvothermal synthesis and photocatalysis towards organic dye degradation, *Mater. Lett.* 100 (2013) 285–288.
- [41] M. Zalas, Synthesis of N-doped template-free mesoporous titania for visible light photocatalytic applications, *Catal. Today* 230 (2014) 91–96.
- [42] J. Tauc, R. Grigorovici, A. Vancu, Optical properties and electronic structure of amorphous germanium, *Phys. Status Solidi (B)* (1966) 627–637.
- [43] E.A. Davis, N.F. Mott, Conduction in non-crystalline systems V. Conductivity, optical absorption and photoconductivity in amorphous semiconductors, *Philos. Mag.* 22 (1970) 0903–0922.
- [44] D.D. Van Slyke, The determination of carbon dioxide in carbonates, *J. Biol. Chem.* 36 (1918) 351–354.
- [45] A. Malygin, V. Ponomareva, Simple chemical method for the determination of carbon dioxide in air, *J. Anal. Chem.* 62 (2007) 16–23.
- [46] J. Akhondzadeh, M. Costas, I. Lavilla, M. Chamsaz, C. Bendicho, Miniaturized and green method for determination of chemical oxygen demand using UV-induced oxidation with hydrogen peroxide and single drop microextraction, *Microchim. Acta* 180 (2013) 1029–1036.
- [47] M. Pan, H. Zhang, G. Gao, L. Liu, W. Chen, Facet-Dependent catalytic activity of nanosheet-assembled bismuth oxyiodide microspheres in degradation of bisphenol A, *Environ. Sci. Technol.* 49 (2015) 6240–6248.
- [48] R. He, J. Zhang, J. Yu, S. Cao, Room-temperature synthesis of BiOI with tailorable (001) facets and enhanced photocatalytic activity, *J. Colloid Interface Sci.* 478 (2016) 201–208.
- [49] H. Li, T. Hu, J. Liu, S. Song, N. Du, R. Zhang, W. Hou, Thickness-dependent photocatalytic activity of bismuth oxybromide nanosheets with highly exposed (010) facets, *Appl. Catal. B Environ.* 182 (2016) 431–438.
- [50] L. Zhu, X. Liu, W. Qin, X. Liu, N. Cai, X. Wang, X. Lin, G. Zhang, D. Xu, Preparation, characterization and electronic structures of Fe-doped TiO₂ nanostructured fibers, *Mater. Res. Bull.* 48 (2013) 2737–2745.
- [51] J.B. Condon, Chapter 1 – an overview of physisorption, in: J.B. Condon (Ed.), *Surface Area and Porosity Determinations by Physisorption*, Elsevier Science, Amsterdam, 2006, pp. 1–27.
- [52] N.I. Kapustina, A.Y. Popkov, R.G. Gasanov, G.I. Nikishin, Oxidation of secondary cyclic alcohols by Pb(OAc)₄ catalyzed by Cu(II) compounds, *Bull. Acad. Sci. USSR Div. of Chem. Sci.* 37 (1988) 2095–2099.
- [53] L. Eberson, Inverted spin trapping – reaction between the radical cation of alpha-phenyl-N-tert-butylnitronite and ionic and neutral nucleophiles, *J. Chem. Soc. Perkin Trans. 2* (1992) 1807–1813.
- [54] S. Dikalov, R. Mason, Spin trapping of polyunsaturated fatty acid-derived peroxy radicals: reassignment to alkoxy radical adducts, *Free Radic. Biol. Med.* 30 (2001) 187–197.
- [55] S. Dikalov, R. Mason, Reassignment of organic peroxy radical adducts, *Free Radic. Biol. Med.* 27 (1999) 864–872.
- [56] E. Janzen, P. Krygsman, D. Lindsay, D. Haire, Detection of alkyl, alcoxyl, and alkyperoxy radicals from the thermolysis of azobis(isobutyronitrile) by ESR spin trapping – evidence for double spin adducts from liquid-phase chromatography and mass-spectroscopy, *J. Am. Chem. Soc.* 112 (1990) 8279–8284.
- [57] M.V. Merritt, R.A. Johnson, Spin trapping alkylperoxy radicals, and superoxide-alkyl halide reactions, *J. Am. Chem. Soc.* 99 (1977) 3713–3719.
- [58] C. Jones, M. Burkitt, EPR spin-trapping evidence for the direct, one-electron reduction of tert-butylhydroperoxide to the tert-butoxyl radical by copper(II): paradigm for a previously overlooked reaction in the initiation of lipid peroxidation, *J. Am. Chem. Soc.* 125 (2003) 6946–6954.
- [59] M. Conte, X. Liu, D. Murphy, K. Whiston, G. Hutchings, Cyclohexane oxidation using Au/MgO: an investigation of the reaction mechanism, *Phys. Chem. Chem. Phys.* 14 (2012) 16279–16285.